A mechanistic understanding of the modes of Ca^{2+} ion binding to the SARS-CoV-1 fusion peptide and their role in the dynamics of host membrane penetration

Juliana Debrito Carten [1±], George Khelashvili [4,5±], Miya K. Bidon[1], Marco R. Straus [2], Tiffany Tang [1], Javier A. Jaimes [2], Harel Weinstein [4,5*], Gary R. Whittaker [2,3*], and Susan Daniel [1*]

[1] Robert Frederick Smith School of Chemical and Biomolecular Engineering, Cornell University, Ithaca, NY, USA

[2] Departments of Microbiology & Immunology and [3] Public & Ecosystem Health, Cornell University, Ithaca, NY, USA

[4] Department of Physiology & Biophysics, Weill Cornell Medicine, New York, NY, USA

[5] Institute for Computational Biomedicine, Weill Cornell Medicine, New York, NY 10065, USA

*Corresponding author:

*Susan Daniel: sd386@cornell.edu

Gary Whittaker: grw7@cornell.edu

Harel Weinstein: haw2002@med.cornell.edu

[±] These authors contributed equally.

Abstract

The SARS-CoV-1 spike glycoprotein contains a fusion peptide (FP) segment that mediates fusion of the viral and host cell membranes. Calcium ions are thought to position the FP optimally for membrane insertion by interacting with negatively charged residues in this segment (E801, D802, D812, E821, D825, and D830); however, which residues bind to calcium and in what combinations supportive of membrane insertion are unknown. Using biological assays and molecular dynamics studies, we have determined the functional configurations of FP-Ca^{+2} binding which promote membrane insertion. We first mutated the negatively charged residues in the SARS CoV-1 FP to assay their role in cell entry and syncytia formation, finding that charge loss in the D802A or D830A mutants reduced syncytia formation and pseudoparticle transduction. Interestingly, the D812A mutation led to increased pseudoparticle transduction, indicating the Ca^{2+} effect depends on binding at specific FP sites. To interpret mechanistically these results and learn how specific modes of FP-Ca^{2+} binding modulate membrane insertion, we performed molecular dynamics simulations. Preferred residue pairs for Ca^{2+} binding were identified (E801/D802; E801/D830; D812/E821) which promote FP membrane insertion. In contrast, binding to residues E821/D825 inhibited FP membrane insertion, which is also supported by our biological assays. Our findings show that Ca^{2+} binding to SARS-CoV-1 FP residue pairs E801/D802 and D812/E821 facilitates membrane insertion, whereas binding to the E801/D802 and D821/D825 pairs is detrimental. These conclusions provide an improved and nuanced mechanistic understanding of calcium binding modes to FP residues and their dynamic effects on host cell entry.

42 Coronaviruses (CoVs) are a diverse family of enveloped single-stranded RNA viruses
43 responsible for causing respiratory and enteric diseases across a wide range of species (1, 2).
44 Three human coronaviruses have posed significant public health threats during the early 21st
45 century: the severe acute respiratory syndrome coronavirus (SARS-CoV-1) in 2002, (3), Middle
46 East respiratory syndrome coronavirus (MERS-CoV) in 2012 (4), and currently SARS-CoV-2 (5, 6).
47 SARS-CoV-2 vaccines have proven to be highly effective at preventing morbidity and death
48 during the pandemic; however, current experience demonstrates that there is an ever-present
49 need for antivirals as a parallel line of defense. Development of such therapeutics requires a
50 better understanding of the fundamental biology of coronaviruses and the intrinsic and
51 extrinsic determinants of viral entry.

52 Infectivity by coronaviruses is mediated by the highly conserved and complex spike (S)
53 glycoproteins, which form homotrimers in the virion membrane and interact with host cell
54 receptors, such as angiotensin-converting enzyme 2 (ACE2) or DPP4 (7) during the entry
55 process. Upon spike-mediated interaction with the host cell surface receptor, CoVs are
56 proposed to utilize two different entry pathways: an “early” route involving proteolytic priming
57 at the cell surface and a “late” route that follows the canonical endosomal/lysosomal pathways
58 (8). The entry pathway utilized is largely dependent on the local protease environment (9, 10).
59 Previous work has shown that SARS-CoV-1 can enter host cells via the early pathway when the
60 transmembrane serine protease 2 (TMPRSS2) and the virus receptor ACE2 are both present in
61 the plasma membrane, or when activated by exogenous trypsin after binding to the cell surface
62 (11). SARS-CoV-1 can also enter cells via the endosomal route where low pH-dependent
63 proteases, such as cathepsin L, cleave and prime the FP for membrane insertion and fusion. This

64 latter pathway is likely the predominant one used by SARS-CoV-1 in most laboratory cell lines
65 used thus far (*e.g.* Vero cells)(9, 10, 12).

66 The entry flexibility seen across coronaviruses arises from the differential requirements for
67 protease priming and activation of the S protein. The SARS-CoV-1 S protein contains proteolytic
68 cleavage sites that enable its spatial and temporal regulation throughout the viral life cycle (9).
69 Two well-characterized protease sites, S1/S2 (R667) and S2' (R797), are specifically involved in
70 SARS-CoV-1 FP activation. The S1/S2 site resides at the boundary between the S1 (receptor
71 binding) and S2 (fusion) domains of the spike and is cleaved by trypsin-like proteases or
72 cathepsin (9, 13, 14). The S2' prime site is located adjacent to the N-terminus of the FP and
73 cleavage at this residue allows the S2 domain to undergo a large conformational change that
74 favorably positions the FP for insertion into the host cell membrane (12).

75 In addition to protease priming, it is known that several viral fusion glycoproteins need
76 calcium ions to initiate membrane fusion during viral entry. The Rubella virus spike glycoprotein
77 (E1) was the first calcium-dependent viral fusogen discovered, with calcium found to play a role
78 specifically on E1 membrane insertion and fusion (15). Subsequent studies done by our group
79 with Zaire Ebolavirus (16), SARS-CoV-1 (17), and MERS-CoV (18) have shown that calcium
80 interacts directly with viral fusogens and is a conserved feature across several different viral
81 entry pathways. In work done with the SARS-CoV-1 and MERS-CoV FPs, calcium was also found
82 to induce membrane ordering in a calcium-dependent manner following FP membrane
83 insertion, with the stoichiometry between the FP segments and calcium ions predicted to be
84 1:2 for SARS-CoV-1 and 1:1 for MERS-CoV (18). Additionally, the SARS-CoV-1 FP adopts a higher
85 degree of α-helicity in the presence of calcium ions and synthetic membranes (17, 19). Taken

86 together, these results suggest that direct interaction between calcium ions and the SARS-CoV-
87 1 FP residues stabilizes the spike FP to help anchor it in the host cell membrane to promote
88 viral-host membrane fusion.

89 The CoV FP sequence contains several conserved negatively charged amino acids that
90 flank the highly conserved hydrophobic residue motif LLF, which is known to interact with the
91 host cell membrane upon FP insertion (17, 20). We have posited that, like the SARS-CoV-2 FP
92 (21), the SARS-CoV-1 FP binds to calcium at these negatively-charged residues to stabilize its
93 local structure and position it for optimal membrane penetration (17, 19, 21). However, we lack
94 a detailed mechanistic understanding of how binding modes of Ca^{2+} to the SARS-CoV-1 FP
95 charged residues facilitates host membrane insertion. The negatively charged residues of the
96 SARS-CoV-1 FP important for calcium binding were identified from a combination of
97 mutagenesis studies (22) and biophysical characterizations (23), which found that when
98 mutated, these residues' interactions with calcium were affected to varying degrees.

99 Here we first systematically examine the effects of mutating charged residues in the
100 SARS-CoV-1 FP on functional metrics consisting of syncytia formation and pseudoparticle
101 transduction, two assays which assess membrane fusion and entry, in cultured cells. We chose
102 SARS-CoV-1 as a prototype beta CoV model FP as it has the best prior analysis of structure-
103 function relationships. We then used atomistic molecular dynamics (MD) simulations of the
104 corresponding SARS-CoV-1 FP molecular systems to determine where Ca^{2+} binds preferentially
105 and how these modes of binding affect FP membrane insertion. The analysis of the preferred
106 loci of Ca^{2+} binding for the wild type and mutated FP segments identified two residue pairs
107 where Ca^{2+} binding was observed to promote FP membrane insertion (E801/D802; D812/E821),

108 and one pair where Ca^{2+} binding inhibits insertion (E821/D825). Experimental probing using
109 biological assays largely confirmed these predictions. Our interpretations of these results
110 enabled us to propose two modes of SARS-CoV-1 FP membrane penetration modulated by FP-
111 calcium interactions: (Mode 1) Binding of Ca^{2+} to FP residue pairs E801/D802 and D812/E821
112 supports insertion of the LLF-containing segment by shielding the neighboring negative charges
113 from repulsion by the phospholipid headgroups, and (Mode 2) Binding of Ca^{2+} to FP residue pair
114 D821/D825 stabilizes a conformation that leaves unshielded anionic residues in the LLF-
115 containing insertion region, which is unfavorable for membrane penetration. These
116 mechanistic inferences from our combined biological and computational investigation provide
117 an atomistically nuanced understanding of how specific FP residues interact with calcium ions
118 to drive host membrane insertion during SARS-CoV-1 infection.
119

120 **Results**

121 **Generation and characterization of SARS-CoV-1 Spike fusion peptide mutants**

122 Various structural conformations of the SARS-CoV-1 spike monomer have been determined
123 using Cryo-EM (PDB: 5XLR, 5WRG, 5X58) (24). In these pre-fusion structures, the fusion peptide
124 (FP) segment containing the core hydrophobic residues LLF appears to adopt an α-helical
125 conformation, followed by a proximal disordered loop known to participate in cysteine-
126 mediated intramolecular disulfide bonding **(Fig 1A).** The 6 negatively charged residues (E801,
127 D802, D812, E821, D825, D830) in this SARS-CoV-1 FP segment are highly conserved across
128 SARS-CoV-1, MERS-CoV, and SARS-CoV-2 **(Fig 1B).**
129

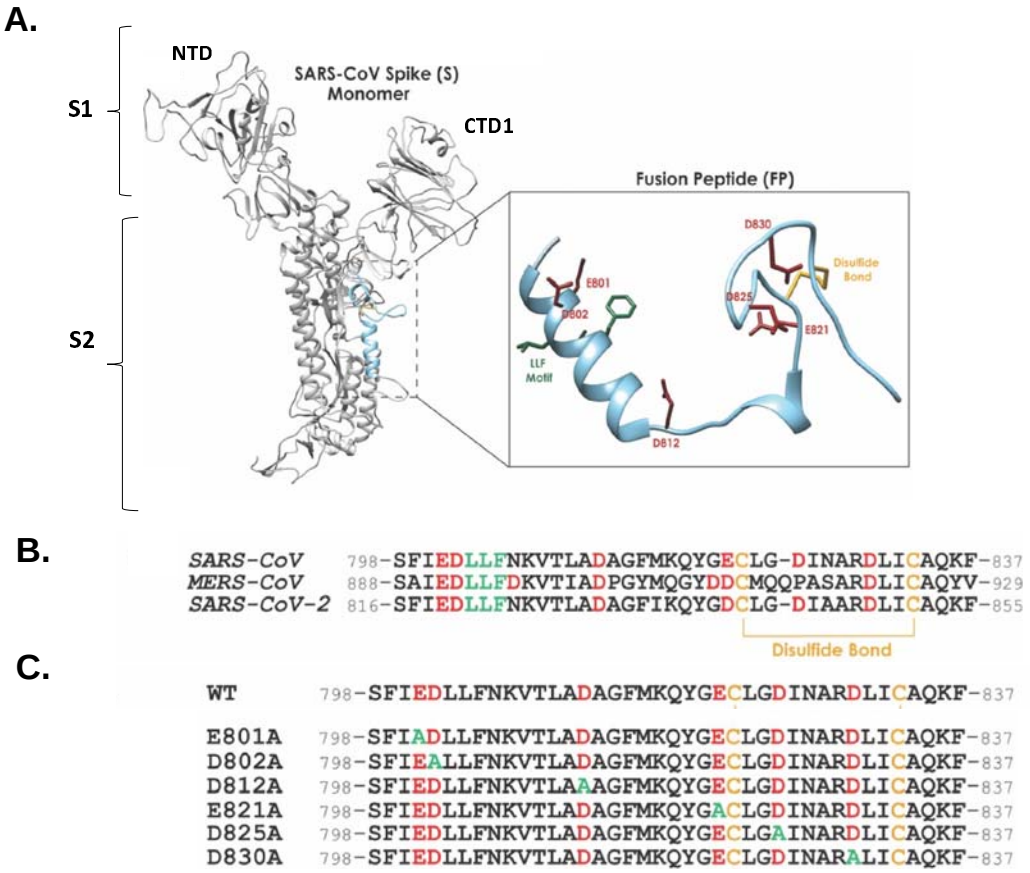

Figure 1. Structure of WT SARS-CoV-1 spike monomer, the fusion peptide region, and the amino acid sequences of the S constructs generated in this study (A) The monomeric SARS-CoV-1 spike glycoprotein in the prefusion conformation (Gui et al. 2017; PDB: 5XLR). The β strand-rich S1 subunit of the spike protein contains the C-terminal domain 1 (CTD1), which mediates ACE2 receptor binding, and the N-terminal domain (NTD). The S2 subdomain contains mostly α-helices and is comprised of two heptad repeat regions (HR1 and HR2) and the fusion peptide (FP). The fusion peptide is highlighted in light blue and expanded to show its predicted structure and residues of interest in this study. The hydrophobic LLF residues appear in green, negatively charged residues in red, and the disulfide bond in yellow. (B) Alignment of the amino acid sequences of SARS-CoV-1, MERS-CoV, and SARS-CoV-2 FPs showing the hydrophobic LLF motif (green), the negatively charged residues (red), and the intramolecular disulfide bond. (C) The 40-amino acid long sequence of the SARS-CoV-1 WT FP (GenBank accession no. AAT74874.1). Charged residues appear in red, alanine substitutions appear in green, and cysteine residues appear in yellow.

147 To determine the functional roles of these negatively charged residues and their involvement in
148 the binding of Ca^{2+} during viral entry, we generated single and double alanine substitutions of
149 these residues. We first made single amino acid (aa) substitutions (E801A, D802A, D812A,
150 E821A, D825A, D830A) in the wild-type SARS-CoV-1 FP. The wildtype and mutant forms of the
151 SARS-CoV-1 S gene were then cloned into pcDNA3.1 expression vectors to enable their
152 transient expression and characterization. To verify the synthesis of folded and active protein,
153 we assessed the ability of the spike (S) protein to be appropriately cleaved for fusion activation.
154 To achieve this, 24 hours after transfection, HEK293T cells were incubated with TPCK-trypsin
155 (1ug/mL) for 10 minutes. Cell surface S proteins were biotinylated and retrieved following cell
156 lysis with streptavidin beads, resolved by gel electrophoresis, and immunoblotted for using a
157 SARS-CoV-1 S polyclonal antibody. The resulting spike immunoblots displayed the full-length,
158 uncleaved S species (S_0) migrating at ~185kDa in untreated samples (**SI Fig S1 A, odd lanes**).
159 SARS-CoV-1 S mutants containing the single mutations D802A, E821A, D825A, and D830A had
160 comparable cell surface levels of S protein to the wild-type protein, indicating that these
161 mutants are not impaired in their synthesis or trafficking to the plasma membrane.
162 Additionally, proteolytic cleavage of all mutants occurred following treatment with Trypsin,
163 indicating that these mutants had accessible cleavage sites and were able to be primed for
164 downstream fusion evens (**SI Fig S1 A, even lanes)**. The two lower molecular weight bands that
165 appear at ~100kDa and ~80kDa in the TPCK-trypsin treated lanes are the S_1 and S_2 subunits,
166 which are generated following cleavage presumably at the S1/S2 site (**SI Fig S1**, black arrows).
167 These subunits have been detected previously following cleavage of a recombinant S protein
168 monomer by Trypsin at the S1/S2 cleavage site (25). We note that we were unable to detect

169 surface levels of the E801A mutant on the spike immunoblots (data not shown). To further
170 probe the nature of this residue's importance for S protein stability, we substituted it with the
171 larger, nonpolar methionine (E801M), a polar and uncharged glutamine (E801Q), a positively
172 charged lysine (E801K) and the charge mimetic aspartic acid (E801D). None of these mutations
173 restored the cell surface levels of the S protein to that of wild-type (data not shown), indicating
174 the specific requirement of glutamic acid in this region of the FP.
175
176 **Analysis of the SARS-CoV-1 FP single mutant pseudoparticles' ability to transduce cells**
177 We next tested the ability of the SARS-CoV-1 single mutants to facilitate host cell entry
178 using SARS-CoV-1 pseudoparticles as a surrogate for infectious virus. This was necessary
179 because SARS-CoV-1 is designated a Risk Group 3 Select Agent which requires experiments to
180 be carried out in a specialized biosafety level 3 (BSL-3) facility. The pseudoparticles offer a safe
181 alternative to live SARS-CoV-1 virus work and enable experiments to be done in BSL-2 level
182 conditions (26). To generate SARS-CoV-1 pseudoparticles in HEK293T cells, we used a three-
183 plasmid co-transfection system with plasmids encoding: (1) the full length CoV-1 surface S
184 protein, (2) the murine leukemia virus (MLV) core proteins *gag* and *pol*, or (3) a firefly luciferase
185 reporter gene containing the MLV-MJ RNA packaging signal and flanked by long terminal repeat
186 (LTR) sequences (26). Upon successful pseudoparticle fusion with the host cell membrane, the
187 luciferase reporter RNA transcript is reverse transcribed, integrated into the cellular genome,
188 and expressed – which enables a measurable readout of pseudoparticle entry via luciferase
189 activity. Our previous studies have shown that this approach works well for assessing the
190 infectivity of MERS-CoV (18), SARS-CoV-1 (17, 26), and SARS-CoV-2 (27) pseudoparticles.

Incorporation of the WT and mutant S proteins into the SARS-CoV-1 pseudoparticles was assessed via Spike immunoblotting of the harvested pseudoparticles. Pseudoparticles with WT or the mutant S proteins D802A, D812A, E821A, D825A, and D830A displayed S protein incorporation, with bands at ~185 kDa (S_0) representing full-length monomeric S protein appearing in all lanes (**Fig 2A**).

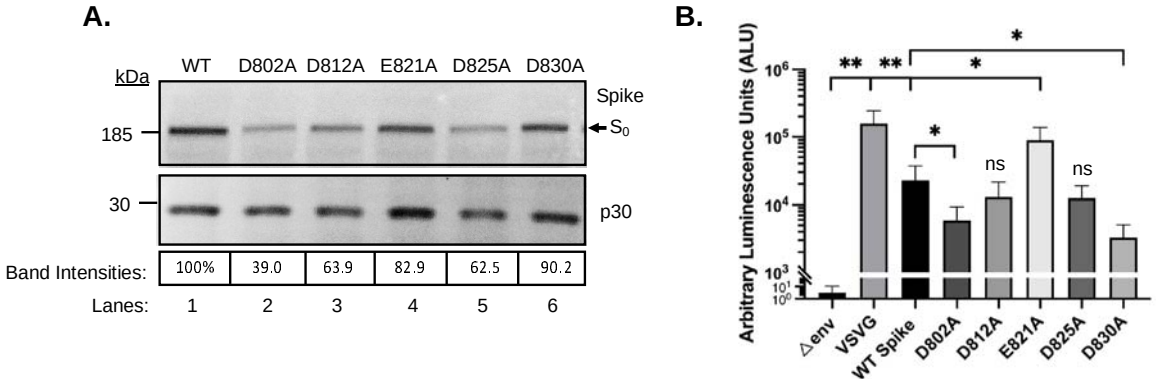

Figure 2. Immunoblot analysis and transduction assays of wild-type and single mutant SARS-CoV Spike-containing pseudoparticles. (A) Representative Spike and p30 immunoblots of pseudoparticles containing wild-type (WT, lane 1) or single charge-to-alanine spike mutants (lanes 2 to 6). S_0 indicates the full-length, uncleaved spike protein. MLV p30 was used as a loading control. Spike and p30 band intensities from 2 sets of blots done with a single batch of pseudoparticles were quantified using ImageJ. Band intensities were normalized to WT and appear as percentages below the blot lanes. (B) WT and mutant SARS-CoV-1 pseudoparticle transduction assays in VeroE6 cells. VSVG-typed and delta envelope (Δenv) pseudoparticles were used as positive and negative controls respectively. * and ** denote a significance of $p \leq 0.05$ or $p \leq 0.01$, respectively. Graph represents 5 technical replicates of the same batch of pseudoparticles. The transduction assay was repeated with a second batch of pseudoparticles with a minimum of 3 technical replicates.

Spike band intensities were quantified relative to the loading control (p30) and then normalized to the WT spike band, which was set to 100%. All of the single mutant-containing pseudoparticles had reduced levels of full-length spike to varying degrees (**Fig. 2A**). The D802A mutant had the least amount of full-length Spike (39.0%), followed by the D812A (63.9%) and D825A (62.5%) mutants. For the E821A and D830A mutants we measured, only minor

214 decreases in Spike levels were observed at 82.9% and 90.2%, respectively. This variability in
215 fusogen levels across the pseudoparticles generated was considered when interpreting the
216 results of the transduction assay. After confirming the incorporation of the spike proteins into
217 the SARS-CoV-1 pseudoparticles, we tested their ability to enter permissive cells. Exposure of
218 VeroE6 cells to WT SARS-CoV-1 pseudoparticles results in a robust luminescent signal 72 hours
219 post transduction, indicating successful pseudoparticle and cell membrane fusion (**Fig 2B**).
220 Pseudoparticles containing the D812A and D825A Spike mutants exhibited luminescence values
221 comparable to WT levels, indicating that these individual mutations do not affect cell entry
222 despite containing ~63% of the WT levels of Spike (**Fig 2A, lanes 3 and 5**). In comparison, the
223 D802A and D830A mutant pseudoparticles showed a decrease in cell transduction, resulting in
224 3.8- or 6.8-fold reduction in luminescence values, respectively. It should be noted that the
225 D802A pseudoparticles had the greatest reduction in Spike levels (39%), which may have
226 contributed to the low luminescence values we observed in the transduction assay. Somewhat
227 surprisingly, the E821A-containing pseudoparticles showed a 3.9-fold increase in luminescence,
228 suggesting that this FP mutation enhances cell entry.
229
230 **Analysis of the SARS-CoV-1 FP mutants' ability to promote syncytia formation**
231 Functional tests of the ability of S mutants to induce cell-cell fusion were performed
232 using a standard technique in the field known as a syncytia assay. Syncytia are multinucleated
233 cells that form following the fusion of neighboring cells during SARS-CoV-1 infection and are
234 one of several pathological hallmarks of cellular dysfunction induced by viral infection(28, 29).
235 To perform this assay, WT or mutated S constructs were transiently transfected into VeroE6

236 cells, a kidney epithelial cell line that expresses the ACE2 receptor (30). 24 hours following
237 transfection, cells were treated with TPCK-Trypsin (2ug/mL) to cleave the FP at the S1/S2 site
238 and induce cell-cell fusion. Syncytia were visualized by immunofluorescence using a SARS-CoV-
239 1 S antibody and cells were co-stained with DAPI to identify multinucleated cells. Cells
240 transfected with WT SARS-CoV-Spike and left untreated served as a negative control for
241 syncytia formation. Syncytia were quantified by counting every group of fused cells with a
242 minimum of 4 nuclei and expressed as a percentage of the total number of generic fluorescent
243 particles counted in a field of view (yes/no binary binning method). VeroE6 cells expressing the
244 WT S readily formed syncytia with an average of ~45.1% of fluorescent regions of interest
245 (ROIs) being classified as syncytia (**Fig 3**). Similarly, VeroE6 cells expressing the E821A (40.3 %
246 syncytia) or D825A (43.7% syncytia) Spike mutants exhibited comparable syncytia formation to
247 cells expressing WT S, indicating that loss of a negative charge in these individual residues does
248 not affect FP function (**Fig 3)**. Conversely, cells expressing the D802A, D812A, and D830A Spike
249 show defective syncytia formation, with the D802A (13.5 % syncytia) and D830A (9.8 %
250 syncytia) mutants showing a major reduction in syncytia formation, similar to the untrypsinized
251 controls (9.3% syncytia). The D812A mutation moderately decreased syncytia formation to 34%,
252 indicating that this FP residue is less important in mediating cell-cell fusion events.

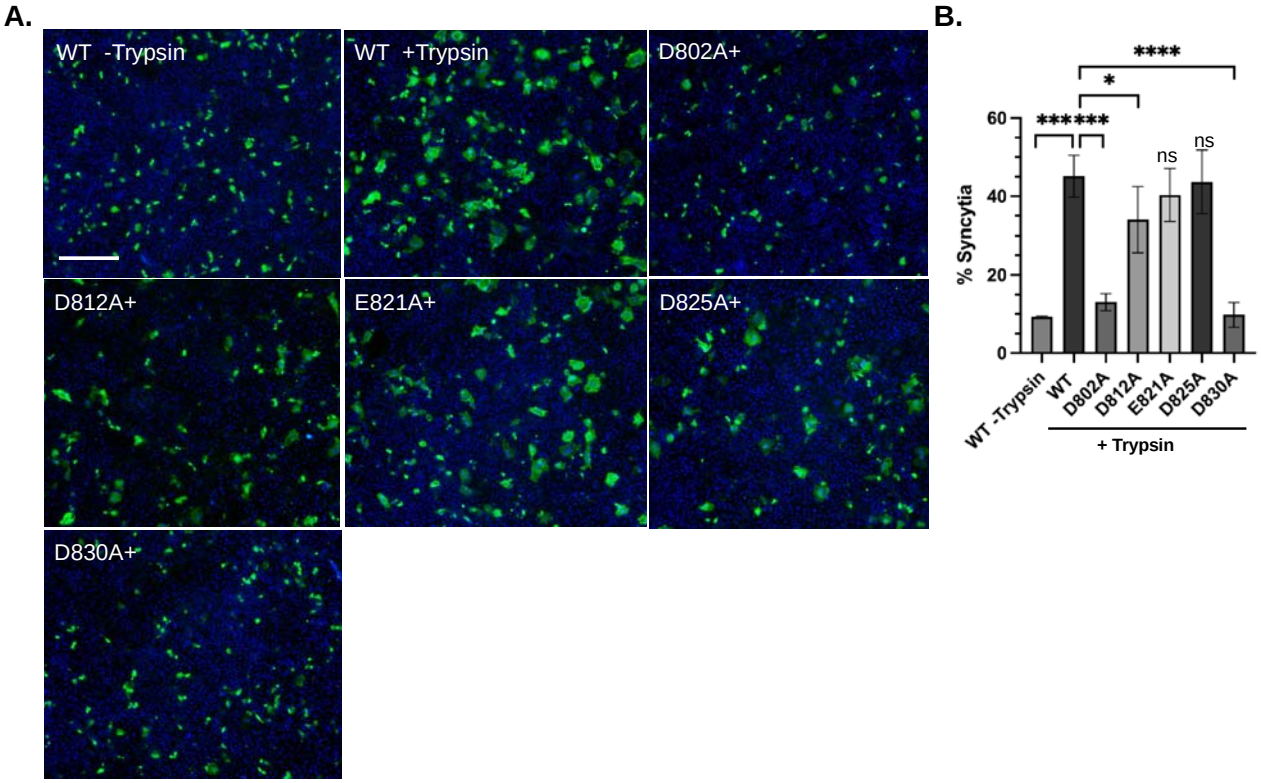

Figure 3. Syncytia formation in SARS-CoV-1 wild-type and single charge-to-alanine mutant S-expressing VeroE6 cells. (A) Representative immunofluorescence images of VeroE6 cells expressing WT or single charge-to-alanine mutant S constructs. 24 h following transfection, cells were left untreated (-Trypsin) or treated with 2ug/mL TPCK-Trypsin (+ Trypsin or +) for 5 minutes to cleave S proteins and induce syncytia formation. Cells were then fixed the following day and syncytia were visualized using a SARS-CoV-1 S antibody (*green*). Nuclei were stained with DAPI and appear in blue. Images were taken at 20X magnification. Scale bars = 90 µm (B) Quantification of syncytia across each condition. *, ***, and **** denote a significance of $p < 0.05$, 0.001, and 0.0001, respectively. n = 3 to 6 biological replicates.

Molecular Dynamics simulations identify the modes of the SARS-CoV-1 FP's calcium binding

The major effects on cell-cell fusion and cellular transduction observed for the mutant SARS-CoV-Spike FP constructs confirmed their importance for viral entry processes at the level of membrane fusion. To test the relationship between the preferred modes of FP residue-calcium binding and membrane insertion, we carried out atomistic molecular dynamics (MD) simulations of the various SARS-CoV-1 FP constructs in the presence of Ca^{2+} ions. This enabled us to systematically compare the mutagenesis results and deduce a potential mechanism of FP

270 membrane insertion. Notably, this also allowed us to examine the mutation of residue E801,
271 which could not be included in the experimental investigations, as described above.

272 To monitor the spontaneous binding of calcium to the FP, we collected 18 independent MD
273 trajectories of 640ns in length for each construct. Following the analysis protocols described
274 recently for SARS-CoV-2 FP simulations (21, 31), the various modes of interactions between the
275 SARS-CoV-1 FP and calcium ions were assessed in the trajectories by monitoring: i) the
276 distances between the calcium ions in solution and the side chains of all acidic residues in the
277 peptide; and ii) the pairwise distances between the side chains of all acidic residues.
278 Summarized in **SI Figs S2 and S3** are the observed events of simultaneous association of two
279 calcium ions with various pairs of FP residues in the individual trajectories of the WT and the
280 mutant systems (see *red* and *blue* rectangles). The combined statistics for each construct (*i.e.,*
281 the total number of binding events for different pairs of residues) are summarized in **Fig 4**.
282 These results show the modes of calcium coordination in the WT protein, identifying the most
283 frequent modes involving residue pairs E821/D825 (5 out of 18); E801/D802 and E801/D830
284 (4/18 each); and D812/E821 (2/18). Notably, a similar pattern of coordination preference was
285 observed in our recent computational studies of calcium association with SARS-CoV-2 FP (21).
286 Moreover, simultaneous binding of calcium ions to the SARS-CoV-2 FP residue pairs equivalent
287 to E801/D802 and D812/E821 produced the peptide conformations suitable for membrane
288 penetration. In contrast, conformations that stabilized calcium binding to residues equivalent to
289 the E821/D825 pair did not enable sustained bilayer insertion.

290

291

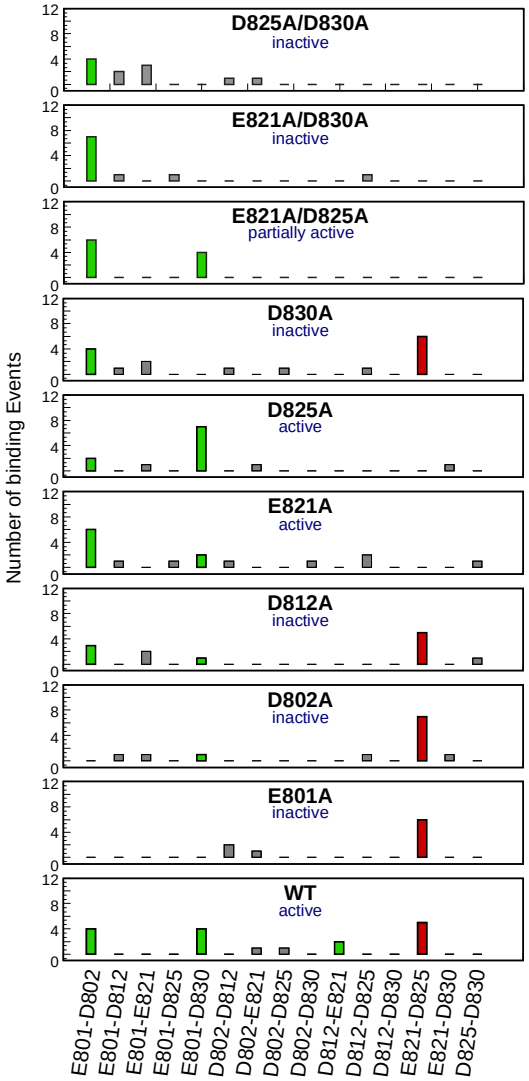

Figure 4. Predicted modes of Ca^{2+} and SARS-CoV fusion peptide binding. Number of Ca^{2+} binding events to different pairs of anionic residues in SARS-CoV FP in the simulations of the WT and the mutant constructs (labeled in each panel). The experimentally measured phenotypes for each construct are shown (active or inactive). The mode of Ca^{2+} ion association predicted to be inhibitory for membrane insertion (E821-D825) is shown in *red*, and the modes of Ca^{2+}association predicted to facilitate membrane insertion are depicted in *green*.

From these MD simulations of the SARS-CoV-1 FP constructs, we were able to predict the phenotypes for each construct (active, partially active, or inactive). The mode of calcium ion association predicted to be inhibitory for membrane insertion (E821-D825) is shown in *red*, and

303 the modes of calcium association predicted to facilitate membrane insertion are depicted in
304 *green* boxes (**Fig 4**). In those single mutant constructs that were predicted to not have fusion
305 activity (E801A, D802A, D812A, and D830A) we found that the only calcium-coordination mode
306 that persists involves the E821/D825 pair, but not the D812/E821 pair of residues (**Fig 4**).
307 Conversely, in the SARS-CoV-1 FP single mutants that maintained WT-like fusion activity (E821A
308 and D825A), we did not observe the E821/D825 residues to participate in calcium binding. In
309 these function-preserving mutants we identified additional modes of calcium binding that are
310 enhanced in comparison to the WT system: E801/D802 in mutant E821A, or E801/D830 in
311 mutant D825A. For the SARS-CoV-1 FP constructs with multiple mutations, our MD trajectories
312 revealed an overall reduced calcium binding ability (**Fig 4 and SI Fig S3**).
313

314 **SARS-CoV-1 FP propensity for membrane insertion is regulated by modes of calcium binding**

315 Overall, the above computational results reveal that the calcium binding patterns of SARS-
316 CoV-1 FP are very similar to those of SARS-CoV-2 FP (21). On this basis, membrane insertion of
317 the SARS-CoV-1 FP could be expected to be enhanced by the modes of calcium binding
318 involving the E801/D802 and D812/E821 pairs of residues, and to be reduced by the ones
319 involving the E821/D825 pair. To test this premise, we carried out MD simulations of FP
320 constructs with two different modes of binding of the Ca2+ ions to the WT SARS-CoV-1 FP
321 associating spontaneously with the lipid membrane (see **Methods**). In Mode 1, the two calcium
322 ions bind at the E801/D802 and D812/E821 sites; in Mode 2, the calcium ions bind to the
323 E801/D802 and E821/D825 pairs. The membrane interaction of each construct was simulated in
324 36 independent replicates, each run for ~0.9-1.0 μs (see **Methods**).

325 Analysis of these trajectories revealed that, indeed, the Mode 1 FP extensively penetrated
326 the membrane, while the membrane insertion of the Mode 2 FP was negligible. This can be
327 seen from the plots presented in **Fig 5** comparing frequencies of membrane insertion for each
328 SARS-CoV-1 FP residue in the simulations of Mode 1 and Mode 2 structures.

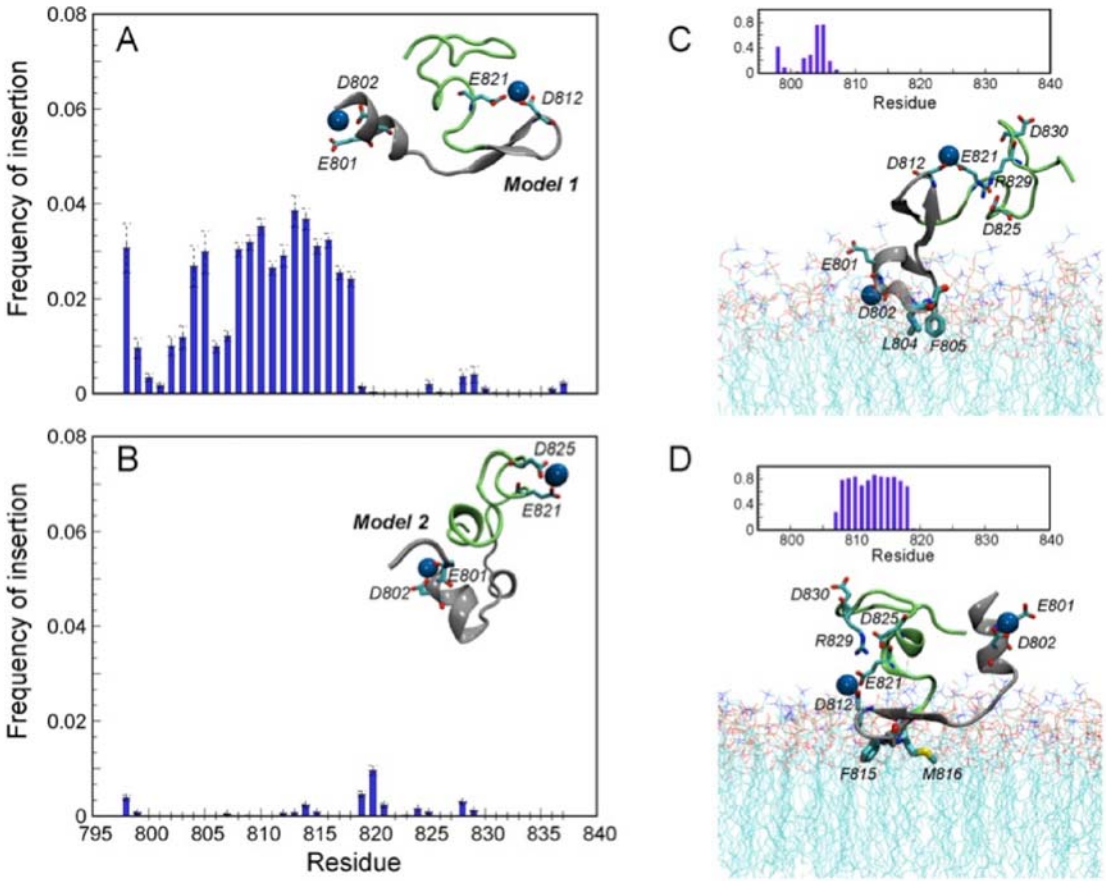

329

330 **Figure 5. Membrane insertion for FP1 and FP2 domains of SARS-CoV fusion peptide.** (A-B)
331 Frequency of membrane insertion for each residue of SARS-CoV FP in the MD simulations of Model 1 (A)
332 and Model 2 (B) constructs, which differ in the mode of Ca^{2+} coordination (see text). The ribbon
333 diagrams in the panels show the corresponding structures. Ca^{2+} coordinating anionic residues are
334 indicated in black text; Ca^{2+} ions are shown as blue spheres. The FP1 and FP2 parts of the fusion peptide
335 are colored in silver and green, respectively. (C-D) The same frequency calculations but done separately
336 for two representative trajectories in Model 1 set in which the observed membrane insertions involved
337 the N-terminal LLF motif (**C**) and the more centrally located (F815-M816) hydrophobic segment (D). The
338 corresponding ribbon diagrams illustrate the structural features of these two distinct insertion modes
339 highlighting (in black) positions of the anionic residues, the hydrophobic residues penetrating the
340 membrane, and the R829 residue interacting with D825. The same color code applies here as in panels
341 A-B.
342

343 The extent of membrane insertion was quantified by monitoring the z-coordinate of the C_α
344 atom of each FP residue, with a residue considered to be inserted into the membrane if the z-
345 distance between its C_α atom and the second carbon atom in the tail of a POPC lipid (atom C22
346 in CHARMM36 notation) was <5Å. There is a strong propensity for bilayer insertion of the
347 fusion peptide with Ca^{2+} binding in Mode 1 (**Fig 5A**), compared to the minimal insertion of the
348 FP with Ca^{2+} binding in Mode 2 (**Fig 5B**). A detailed analysis of individual trajectories in the set
349 of Mode 1 binding, revealed two distinct ways in which these SARS-CoV-1 FP constructs
350 penetrate the membrane, similar to our findings for the SARS-CoV-2 FP (21). In one way, the N-
351 terminal segment containing the LLF motif penetrates the bilayer, as shown in **Fig 5C**; in the
352 other, the more centrally located hydrophobic F815-M816 segment enters the bilayer (**Fig 5D**).
353 Interestingly, the two insertion modes appear to alternate which calcium ion binding site is
354 neighboring the inserted portion. Thus, when the LLF is inserted, the calcium ion associated
355 with the neighboring E801/D802 residues is bound to the membrane while the other calcium
356 binding site (D812/E821) is situated away from the membrane surface (**Fig 5C**). In the case of
357 the F815-M816 insertion, the position of the calcium binding loci with respect to the membrane
358 is reversed – the one associated with the D812/E821 pair is membrane-bound, while the
359 E801/D802 pair is located farther from the bilayer (**Fig 5D**). We also note that in both cases, the
360 remaining anionic residues in the peptide (*i.e.* the ones not engaged with the calcium ions) are
361 either solvent exposed (D830) or engaged in charge-neutralizing interactions with neighboring
362 basic residues (D825/R829) (**Fig 5C and D**). These results support a mechanistic model in which
363 membrane penetration of the SARS-CoV-1 FP is significant only for specific modes of calcium
364 binding to the peptide, i.e., to the E801/D802 and D812/E821 pairs of conserved acidic

365 residues. Moreover, calcium binding at the E821/D825 pair is predicted to inhibit membrane
366 insertion because it leaves charged residues in the vicinity of the hydrophobic conserved LLF
367 unscreened and thus repelled by the negatively charge phospholipid headgroups.
368
369 **Analysis of SARS-CoV-1 FP double mutants using syncytia and pseudoparticle transduction**
370 **assays**
371 We then tested the biological consequences of eliminating pairs of residues from the FP,
372 generating the following double mutants: E821A/D830A, D825A/D830A, and E821A/D825A
373 (**Figure 6A**). As with the single charge-to-alanine S mutants, we validated these mutants by
374 transiently expressing the mutant constructs in HEK-293T cells, biotinylating all cell surface
375 proteins, performing a Steptavidin pulldown, and carrying out spike immunoblots. All three
376 double mutants have comparable cell surface levels of full-length protein compared to WT S,
377 indicating that they are similarly synthesized and trafficked to the plasma membrane (**SI Fig**
378 **S1B, odd lanes**). In addition, the nearly complete disappearance of the full-length mutant S
379 species and the appearance of the S_1 and S_2 subunits following TPCK-Trypsin treatment
380 indicates that these mutants are cleaved similarly to WT S (**SI Fig S1B, even lanes)**.
381 The pseudoparticles containing these double mutants in the SARS-CoV-FP were assayed
382 for incorporation via Spike immunoblotting, which showed that they incorporated their
383 respective S proteins but exhibited variable S protein levels in comparison to the WT
384 pseudoparticles (**Fig 6B**). Transduction assays were then carried out using VeroE6 cells to assess
385 the ability of these pseudoparticles to fuse with and enter host cells. In comparison to WT, the

E821A/D830A and D825A/D830A pseudoparticles showed an 11.7-fold and 23.2-fold reduction in cell transduction, respectively (**Fig 6C**).

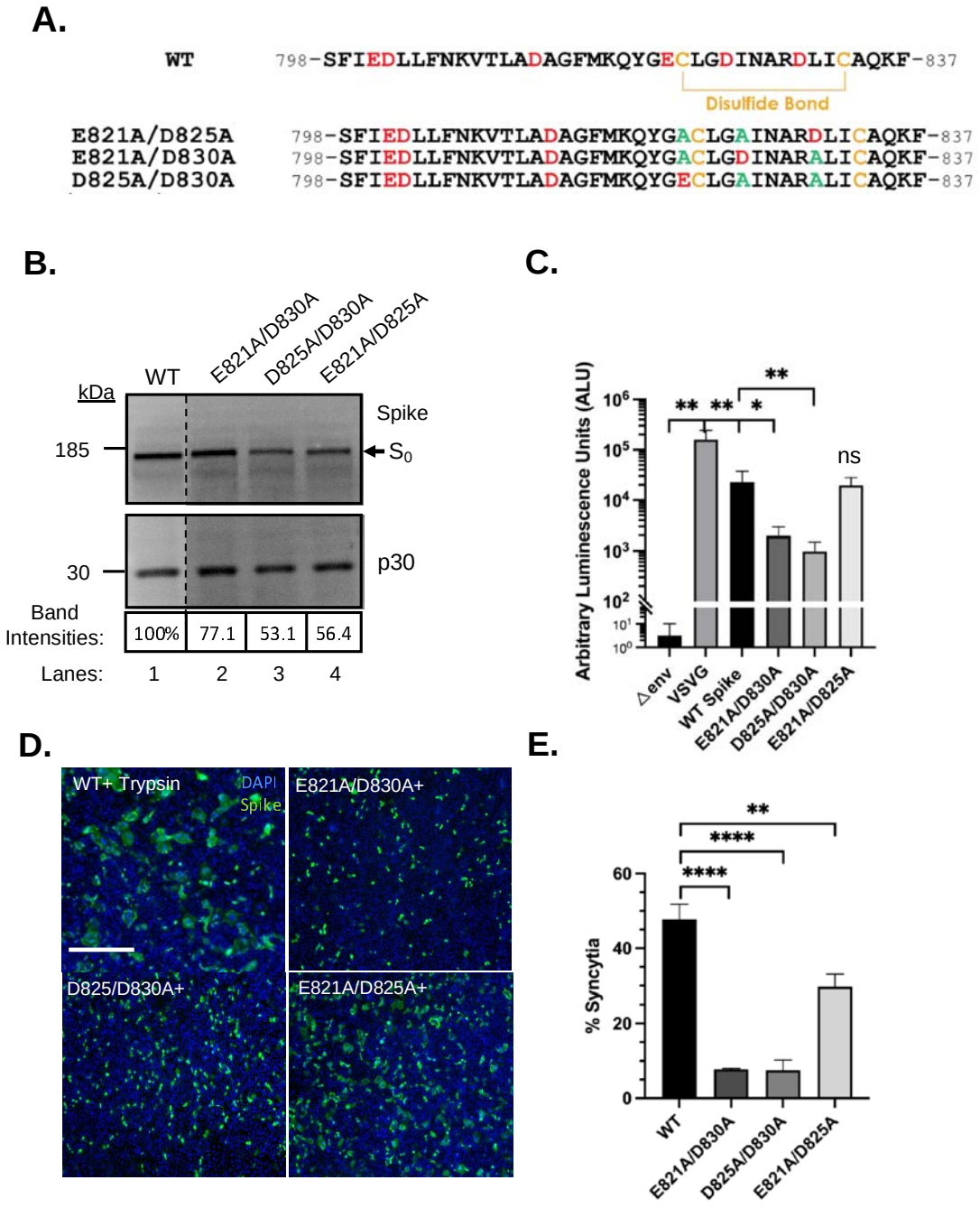

Figure 6. Syncytia formation and pseudoparticle transduction assays of SARS-CoV-1 double mutants. (A) Primary amino acid sequences of the WT and charge-to-alanine SARS-CoV-1 FP double mutants generated (E821A/D830A, D825A/D830A, and E821A/D825A). WT charged residues appear in red, alanine substitutions in green, and cysteine residues in yellow.

394 (B) Representative Spike and MLV p30 immunoblots of pseudoparticles containing WT (lane 1)
395 or double mutant (lanes 2 to 4) SARS-CoV-1 Spike pseudoparticles. S0 indicates the full-
396 length, uncleaved Spike. p30 was used as a loading control. Dashed lines indicate where the WT
397 lanes from the same blots have been reordered for clarity. (C) SARS-CoV-
398 1 pseudoparticle transduction assay in VeroE6 cells with WT and double mutant
399 pseudoparticles. * and ** denote a significance of $p \leq 0.05$ or 0.01, respectively, from
400 luminescence values taken from 3 biological replicates. (D) Representative
401 immunofluorescence images of VeroE6 cells transiently expressing WT or the double mutant
402 (E821A/D830A, D825A/D830A, or E821A/D825A) Spike constructs. 24 h following transfection,
403 cells were treated with Trypsin (+ Trypsin or +) for 5 minutes to cleave S proteins and
404 induce syncytia formation. Syncytia were visualized using a SARS-CoV S antibody (*green*)
405 following cell fixation. Nuclei were stained with DAPI and appear in blue. Images were taken at
406 20X magnification. Scale bars = 90µm. Images were collected from at least 3 independent
407 experiments. (E) Quantification of percent syncytia across the WT and double mutant
408 conditions. Syncytia were defined as any multinucleated cell with 4 or more nuclei. ** and ****
409 denote significance of $p \leq 0.01$ and 0.0001, respectively. n = 3 or 4 biological replicates.
410

411 Given that the D830A single mutation resulted in the greatest reduction in pseudoparticle
412 transduction amongst the single mutants (down 6.8-fold compared to WT pseudoparticles), it is
413 not surprising that the double mutants containing this mutation, in addition to mutations in
414 residues predicted to be non-essential by MDS, remain defective in cell entry. Additionally,
415 these mutant pseudoparticles both had reduced levels of S, which may partially account for
416 their lower cell transduction. In contrast, the E821A/D825A double mutant showed WT-like
417 luminescence values, indicating that mutating both of these residues does not appear to have
418 an effect on pseudoparticle transduction (**Figure 6C**).

419 We then tested the functionality of these S mutants using the previously described
420 syncytia assay. VeroE6 cells transiently expressing the double mutants E821A/D830A (7.8%
421 syncytia) and D825A/D830A (7.5% syncytia) displayed a pronounced defect in syncytia
422 formation (< 10% syncytia) in comparison to WT S-expressing cells (47.7% syncytia) (**Fig 6D and**
423 **E**). The E821A/D825A double mutant exhibited a modest decrease in syncytia formation (29.7%

424 syncytia). We observed the same general trends for the double mutants in the pseudoparticle
425 transduction and syncytia assays, namely that the D830A-containing mutants had the greatest
426 detrimental effect, with the E821A/D825A having a smaller effect on syncytia formation but not
427 on pseudoparticle entry. The results from MD simulations for the SARS-CoV-1 FP double
428 mutants studied experimentally **(Fig. 6)** are consistent with these experimental findings. We
429 found the double mutants have an overall reduced calcium binding ability, i.e., mostly a single
430 calcium ion was binding to the peptide at any given time (see details in **SI Fig S3**). The pattern of
431 calcium binding in the functionally deficient double mutants, E821A/D830A and D825A/D830A,
432 was different from that in the partially active E821A/D825A construct (**Fig. 4**). Thus, in the
433 E821A/D825A mutant, calcium preferentially bound to the E801/D830 pair, which is a preferred
434 mode of binding in the WT as well, while the other two constructs are missing the D830 residue
435 which was shown to be important for function.
436
437 **Discussion**
438 Early structure-function studies of the SARS-CoV-1 FP pointed to peptide regions –
439 especially the largely conserved LLF motif and the residues flanked by cysteines (C822-C833) –
440 as important features for membrane fusion activity (22). In this work, a charge reversal point
441 mutation (D830L) and a deletion of several amino acids including this residue (Δ823-832) were
442 found to have pronounced effects on membrane fusion and pseudoparticle transduction (22);
443 however, these studies were performed before the importance of calcium during viral entry
444 was known and hence their mechanistic importance, described here, was missed. More recent
445 biophysical characterization of the FP has found that mutating residue D812 in the FP1 region

446 has the greatest effect on membrane ordering, calcium-specific FP binding, and calcium-
447 induced FP structural changes (23). Residue D830 in the FP2 region (labeled 831 in the citation)
448 was also found to be important, causing loss of membrane ordering and calcium sensitivity
449 when mutated, as were residues 802 and 801, which they proposed together form a calcium
450 binding site (23).

451 In this systematic study of the roles of the negatively charged residues in the SARS-CoV-
452 1 FP, we first confirmed their importance for pseudoparticle transduction, a proxy we use for
453 viral infectivity. After validating the mutant S proteins (**SI Fig S1**) and confirming their
454 incorporation into pseudoparticles (**Fig 2A**), we found that SARS-CoV-1 pseudotyped particles
455 containing either the Spike D802A or D830A mutation had decreased transduction into VeroE6
456 cells (**Fig 2B**). Conversely, D812A and D825A S-containing pseudoparticles were as able to enter
457 cells as well as their WT counterparts. An interesting finding from this set of experiments is that
458 the E821A mutation enhanced transduction, suggesting that it is advantageous during viral
459 entry. The test of fusion competency of the single FP mutants showed that VeroE6 cells
460 expressing the D802A or D830A mutants exhibited a pronounced cell-cell fusion defect, while
461 the D812A mutant showed a more moderate decrease. The D821A and D825A mutants formed
462 syncytia similar to WT S-expressing cells (**Fig 3**). In summary, our biological data from our single
463 mutants confirm that residues D802 and D830 are essential in a non-redundant manner to the
464 function of the SARS-CoV-1 fusion peptide and that loss of transduction ability in these
465 pseudoparticle mutants is likely due to a defect at the level of membrane fusion.

466 We then conducted MD simulations of the WT and mutant constructs (summarized in
467 **Fig. 4**) to identify the preferred modes of SARS-CoV-1 FP-Ca^{2+}binding and interrogate which

468 negatively charged residues, when bond to calcium, promote membrane insertion (**Figs. S2** and
469 **S3** in **SI**). We anticipated that FP residues D802 and D830 bound to calcium ion would position
470 the FP favorably for membrane insertion, given that their genetic ablation resulted in loss of S
471 protein fusion competency and decreased pseudoparticle transduction. Indeed, in our
472 simulations, FP residues D802 and D830 were predicted to be part of a pairwise interaction
473 with calcium ions that promotes membrane insertion, Furthermore, single mutations in either
474 of these residues were predicted to inactivate the FP. More broadly, the energetically favorable
475 modes of Ca^{2+}-FP binding identified to promote membrane insertion (**Fig. 5**) all spatially
476 organize the FP to encourage its insertion by (i)-charge screening, and (ii) -stabilizing the
477 peptide conformation for penetration of the hydrophobic LLF motif beyond the phospholipid
478 headgroups. Our results from probing the effect of pairwise mutations of the negatively
479 charged residues in the SARS-CoV-1 peptide support the roles of specific pairs of Ca^{2+} binding
480 residues.

481 The results of MD simulations of the double mutant constructs (**Figs 4**) are fully
482 compatible with the expectations from the experimentally validated predictions for the single
483 mutant constructs (**Fig. 3 and Fig. 4**) and the experimental results shown in **Fig. 6**. The depth of
484 insertion measured in the simulated FP-inserted systems, and the determinant role of the
485 calcium ion in facilitating membrane insertion are identical to the findings for the SARS-CoV-2
486 peptide (21) and are in agreement with the experimental measurements of SARS-CoV-1 FP
487 membrane insertion by Lai *et al* (17, 18, 32). That calcium interacts with the same highly
488 conserved, negatively charged residues in the FPs of SARS-CoV-1 and SARS-CoV-2 is not
489 surprising, given the high sequence similarity between the two FPs.

490 The results from the combined experimental and computational probing of SARS-CoV-1 FP-
491 membrane interactions reveal that the propensity of SARS-CoV-1 FP membrane insertion is
492 determined by specific modes of calcium binding. The calcium binding mode that enables the
493 most sustained membrane penetration involves the initial association of the peptide with the
494 bilayer through a calcium binding site located near the N-terminus of the peptide. This site
495 (E801/D802) is made accessible following enzymatic cleavage and is inserted into the
496 membrane in conjunction with the insertion of the juxtaposed hydrophobic segment (the LLF
497 motif). In this process, all anionic residues of the peptide are engaged with calcium ions, or with
498 neighboring basic residues, unless they remain solvent exposed away from the membrane.
499 Based on the preferred modes of calcium-loaded FP interaction with the membrane generated
500 from our MD simulations, we conclude that the binding of calcium following S protein cleavage
501 at the S2' site creates an energetically feasible membrane insertion process. This process
502 consists of the following three steps: (1) steering of the peptide towards the bilayer surface by
503 shielding calcium interactions with the phospholipid headgroups; (2) enabling the conserved N-
504 terminal LLF motif of the FP to reach the hydrophobic layer of the membrane by screening the
505 negative charges of the neighboring residues involved in Ca^{2+} binding; and (3) shielding of FP
506 anionic residues in the preferred inserting-enabling conformation of the peptide to prevents
507 negative charge from interfering with membrane insertion (**Fig 5**). These three components
508 became evident from the MD simulations that identified the most likely modes of Ca^{2+} binding,
509 the preferred conformations adopted by Ca^{2+} loaded FPs, and the effect of the mutations on
510 these properties and insertion probabilities.

511 Not only do the molecular mechanisms presented here for the SARS-CoV-1 FP bear a very
512 high similarity to results from computational studies of the SARS-CoV-2 FP (21), but in both the
513 SARS-CoV-2 FP simulations (33) and here, we observed a Ca^{2+} binding mode that inhibits stable
514 membrane insertion. In this mode, calcium association with the E821/D825 pair (corresponding
515 to the D839/D843 in SARS-CoV-2 FP) positions the LLF motif near the negatively charged D812
516 residue at the membrane surface (**Fig 5B**). This eliminates the favorable effect of the negative
517 charge screening by the calcium, so that the peptide bilayer encounters are transient and do
518 not lead to penetration by the LLF motif. This mechanistic model, which highlights the role of
519 the positioning of the D812 residue in specific calcium binding modes, is supported by our
520 findings for the SARS-CoV-1 S mutants, as it was previously found to be an impactful mutation
521 in the SARS-CoV-1 FP (20). Furthermore, we directly tested the biological consequences of
522 generating the single and double E821A/D825A mutants, observing that although the E821A
523 mutant pseudoparticles showed an increase in transduction, the single D825A single mutant
524 and E821A/D825A double mutant did not (**Fig 6E**).
525 Indeed, data in **Figs 4** and **5** show that mutations that create a high propensity for the
526 calcium binding mode involving the E821/D825 pair, stabilize peptide conformations that are
527 non-productive for membrane penetration and are found here to inactivate the FP. Current
528 studies on SARS-CoV-2 S protein classified the disordered portion of the FP in the FP2 domain
529 as the FPPR (fusion peptide proximal region), which includes the charged residues
530 D839/D843/D848 or E821/D825/D830 equivalent in SARS-CoV-1 FP (21, 34). This FPPR region
531 was determined to be important, as it binds to the RBD through the CTD1, and maintains the
532 closed pre-fusion S trimer(34). This is due to the tight packing around the disulfide bond

533 reinforced by a bond between K835 and D848 (K817 and D830 in SARS-CoV-1 FP). The
534 equivalent residue in SARS-CoV-1 FP, based on biological studies, is a critical residue (34).
535 Mutating D830 removes the binding partner of K817, thereby loosening the 'knot' of the
536 structured FPPR in maintaining the closed form of the trimeric S protein (34). Without the
537 reinforcements, we may lose the optimal structural conformation of the S protein upon
538 receptor binding to expose the S2' cleavage site to promote successful proteolytic cleavage.

539 A recent study from Koppisetti *et al* asserts that a calcium ion may be binding to
540 D843/D849 in SARS-CoV-2 FP (corresponding to D825/D830 in SARS-CoV-1 FP); however, as
541 shown from the simulations done in this study and our previous report (21), there is a high
542 likelihood that the second calcium ion will bind to D812/D821 (corresponding to the
543 D830/D839 in SARS-CoV-2 FP) for the maximal membrane penetration (21, 35). We note that
544 the model of membrane insertion proposed by Koppisetti *et al (35)* most aligns with our
545 proposed CoV FP interaction with the bilayer (**Fig 5**), but that NMR studies regarding the
546 membrane interaction with the fusion peptide use bicelles (35) and micelles (36) which are not
547 faithful models for the cell membrane bilayer.

548 More broadly, the E801 and D830 residues are conserved within the CoV family and the
549 D812 residue is conserved within betacoronaviruses (17, 20). The implication is that calcium
550 interactions are a conserved mechanism that serves to better position the FP for membrane
551 insertion. Different coronaviruses exhibit different requirements for calcium; MERS-CoV binds
552 to one calcium ion in its FP1 domain (18), thus, it is important to investigate the role of calcium
553 and FP interactions across the CoV family. Recent work using a FRET-assay has shown that
554 calcium interactions with the fusion peptide may drive the pre- to post-fusion conformational

555 changes in SARS CoV-2 spike (31). The authors of this study showed that alpha and beta
556 coronaviruses display a high sensitivity to calcium; the fusion activity of spike drops
557 precipitously as calcium levels rise or decrease past predicted late endosomal concentrations.
558 The conservation of calcium-binding residues in the FP of many coronaviruses suggests that the
559 CoV fusion mechanisms are essential for function and can serve as potential targets for broad-
560 spectrum antiviral drugs (37-39). Repurposing FDA-approved calcium channel blocking (CCB)
561 drugs to inhibit CoV entry, particularly for SARS-CoV-2, is one option worth exploring. Recent
562 studies have shown that the CCB felodipine, among others, is a potential therapeutic candidate
563 to inhibit SARS-CoV-2 entry (40). CCBs can target conserved viral functions, providing a rapid
564 solution to address new and future SARS-CoV-2 variants. It will be important to identify the
565 mechanisms of CCBs CoV inhibition, as they may directly inhibit a viral target or indirectly
566 inhibit viral entry by affecting host cell processes. Interestingly, SARS-CoV-2 variants have arisen
567 as part of Clade 20A that contain a D839G or D839Y mutation (E821 equivalent in SARS-CoV-1),
568 with this mutation predicted to affect FP-Calcium interactions (41-43). To date, it is not known
569 if there is any selective advantage to the virus conferred by this mutation or whether the
570 emergence of these variants simply represents a founder effect. Future studies will continue to
571 illustrate the role of the spike FP in controlling both emerging and existing coronaviruses.

572 **Conclusion**

573 In the field, how calcium binding specifically impacts the dynamics of coronavirus fusion
574 peptide dynamics during host membrane insertion was lacking. We have taken a two-pronged
575 approach to directly investigate this aspect of SARS-CoV-1 entry, using biological studies in
576 combination with molecular dynamics simulations to identify which anionic FP residues interact

577 with calcium ions. We have also demonstrated how specific pairwise interactions likely impact
578 FP function, and ultimately, virus entry. Interestingly, we have found that multiple binding
579 modes of FP-Ca^{2+} exist, with one mode promoting FP membrane insertion and another
580 inhibiting membrane insertion. Our predictive studies are largely in agreement with the findings
581 of our biological data, demonstrating the power of this cross-disciplinary approach to get at
582 viral entry mechanisms.
583

584 **Materials and Methods**

585 **Cells, plasmids, and reagents.** Human embryonic kidney 293 (HEK293T) and African green
586 monkey kidney epithelial (VeroE6) cells were obtained from the American Type Culture
587 Collection (ATCC, Manassas, VA). Both cell lines were grown in complete DMEM, composed of
588 Dulbecco's Modified Eagle medium (DMEM, CellGro), supplemented with 10% HyClone
589 FetalClone II (GE) and 10 mM HEPES (CellGro), and grown at 37°C with 5% CO_2. The plasmids
590 used for generating pseudoparticles were the pCMV-MLV gag-pol murine leukemia virus (MLV)
591 packaging construct, the pTG-Luc transfer vector encoding the luciferase reporter gene, and the
592 pCAGGS-VSVG plasmids. They were generously provided by Jean Dubuisson (Lille Pasteur
593 Institute, Lille, France) and co-transfected as previously described (26). The plasmid encoding
594 the C9-tagged SARS-CoV-1 spike protein (pcDNA3.1-C9-SARS-CoV-1 S) was provided by Dr.
595 Michael Farzan from the New England Primate Research Center. Recombinant L-1-tosylamide-
596 2-phenylethyl chloromethyl ketone (TPCK)-treated trypsin was obtained from Sigma.
597

598 **Site-directed mutagenesis.** Site-directed mutagenesis was performed on the SARS-CoV-1 spike
599 encoding plasmid, pcDNA3.1-SARS-CoV-1-S, via the QuikChange Lightning site-directed
600 mutagenesis kit (Aligent). PCRs and transformations were performed based on the
601 manufacturer's recommendations. The primers used to generate the SARS-CoV-1 S mutants can
602 be found in the supplementary information (**SI, Table S1**). Mutations were confirmed via Sanger
603 Sequencing at the Cornell University Life Sciences Core Laboratories Center.
604 **Cell Surface Biotinylation Assay.** HEK293T cells were seeded in poly-D-lysine coated 6-well
605 dishes. 24 hours later, cells were transfected with 1.5 ug of WT or mutant SARS-CoV-1 S plasmid
606 using polyethylenimine (PEI) (Thermo Fisher Scientific). Cells were transfected for 24 hours,
607 washed once with 1X DPBS, and then left untreated or treated with 1 ug/mL of TPCK-trypsin in
608 DPBS for 5 minutes at 37°C. Cell surface proteins were then biotinylated by incubating rinsed
609 cells in a biotin-containing buffer (250 ug/mL in PBS) for 20 minutes. The biotin buffer was then
610 replaced with a quenching solution (50mM glycine in DPBS) and incubated for 30 minutes. Cells
611 were then lysed in ice for 15 minutes using a lysis buffer (0.1% Triton in 1x TBS) with protease
612 inhibitors (cOmplete Protease Inhibitor Cocktail). Lysates were collected and spun at 13,000
613 rpm for 10 minutes to pellet insoluble material. The lysates were then incubated overnight at 4°
614 C with equilibrated steptavidin beads to retrieve the biotinylated spike proteins. The captured
615 spike proteins were eluted by boiling the beads in 1x LDS sample buffer in the presence of DTT
616 (NuPAGE) for 10 minutes. Proteins were resolved on 4-12% gradient Bis-Tris gels (NuPAGE) and
617 transferred to PVDF membranes. The SARS-CoV-1 S protein was detected using the SARS-CoV-1
618 S rabbit polyclonal primary antibody (NR-4569, BEI resources) and Alexa Fluor 488-labeled goat

619 anti-rabbit secondary antibody (Invitrogen). The resulting protein bands were visualized using a
620 Chemidoc system with Image Lab image capture software (BioRad).
621
622 **Cell-cell fusion assay.** VeroE6 cells were seeded onto glass slides in a 24-well chamber slides
623 (Millipore). After 24 hours, cells were transfected using Lipofectamine according to the
624 manufacturer instructions. Following 18 hours of transfection, cells were washed with 1X DPBS
625 and Trysinized with 2ug/mL TPCK-trypsin for 5 minutes at 37°C to. Cells were then fixed with 4%
626 paraformaldehyde (PFA) (ThermoFisher) for 15 minutes and washed three times with DPBS. To
627 permeabilize the cells, a 0.1% Triton X-100 in DPBS solution was added to each well and cells
628 were incubated for 5 minutes. After three washes with DPBS, the cells were blocked with 5%
629 normal goat serum for 30 minutes. Cells were again washed and then labeled with SARS-CoV-1
630 S rabbit polyclonal antibody (NR-4569, BEI resources), followed by labeling with Alexa Fluor
631 488-labeled goat anti-rabbit secondary antibody (Invitrogen). The cell nuclei were labeled with
632 a DAPI stain present in the mounting media (DAPI Fluoromount-G, Southern Biotech). Images
633 were acquired using an upright microscope (Echo Revolve) with a 10x objective. To quantify the
634 number of nuclei per syncytia, three randomly selected fields were acquired and spike-
635 expressing cells and syncytia were manually counted. The total number of syncytia we counted
636 and expressed as a percentage of the total fluorescent "particles" that were counted in the
637 image. The data was graphed and statistics were carried out using Microsoft Excel and
638 GraphPad Prism 7.
639 **SARS-CoV-1 pseudoparticle infectivity assay.** SARS-CoV-1 pseudoparticles were produced as
640 previously described (18, 26). Briefly, to generate pseudoparticles 3.5 x10^5 HEK293T cells were

641 seeded in 6-well plates. Pseudoparticles were prepared by transfecting HEK293T cells with 600
642 µg of their respective SARS WT or mutant S plasmids, 800 µg of pTG-Luc plasmid, and 600 µg of
643 pCMV-MLV gag-pol plasmid using polyethylenimine (PEI) as the transfection reagent. The cell
644 supernatant was harvested 48 hours post-transfection, centrifuged at 1200 rpm for 7 minutes
645 to separate the pseudoparticles from residual cellular debris, and filtered through a 0.45 µm
646 syringe filter. The pseudoparticles were stored at -80°C for one freeze-thaw cycle. To perform
647 the pseudoparticle infectivity assay, $5x10^5$ VeroE6 cells were seeded into 24-well plates and
648 infected with 200uL of the pseudoparticle suspension for 72 hrs at 37°C. Cells were lysed for 10
649 minutes at room temperature using the Luciferase cell lysis reagent (Promega). Luminescence
650 readings were performed using a Glomax 20/20 Luminometer system (Promega). Each
651 experiment contained a minimum of three technical replicates and experiments were repeated
652 at least three times. Data analysis was performed using GraphPad Prism 7.
653
654 **Modeling of the SARS-CoV-1 fusion peptide.** The structural model of the SARS-CoV-1 S protein
655 fusion peptide is based on the SARS-CoV-1 S prefusion structure from the Protein Data Bank,
656 PDB 5XLR. The sequence of the SARS-CoV-1 S protein (GenBank accession no. AAT74874.1) was
657 aligned to the PDB 5XLR SARS-CoV-1 structure sequence using Geneious software (**v.2020.1.1**).
658 Structural models of the SARS-CoV-1 S monomer were generated using the Modeller
659 comparative modeling tool (**v.9.23**) within the Chimera software (v.1.13; University of
660 California). Images were created using Adobe Illustrator CC (**v.24.03**).
661

662 **Molecular dynamics (MD) simulations of the SARS-CoV-1 FP in water.** For all the atomistic MD
663 simulations, the SARS-CoV-1 FP segment was capped with neutral N- and C-termini (ACE and
664 CT3, respectively, in the CHARMM force-field nomenclature). Protonation states of all the
665 titratable residues were predicted at pH 7 using Propka 3.1 software (44).

666 For the simulations in water, one copy of the peptide (wild-type or a mutant) was
667 embedded in a rectangular solution box and ionized using VMD tools ("Add Solvation Box" and
668 "Add Ions", respectively) (45). The box of dimensions ~90 Å x 80 Å x 82 Å included a Na^+Cl^- ionic
669 solution as well as 2 Calcium ions, and ~18000 water molecules. The total number of atoms in
670 the system was ~54,540.

671 The system was equilibrated with NAMD version 2.13 (46) following a multi-step protocol
672 during which the backbone atoms of the SARS-CoV-1 FP as well as Calcium ions in the solution
673 were first harmonically constrained and subsequently gradually released in four steps (totaling
674 ~3ns), changing the restrain force constants k_F from 1, to 0.5, to 0.1 kcal/ (mol $Å^2$), and 0 kcal/
675 (mol $Å^2$). These simulations implemented all option for rigidbonds, 1fs (for k_F 1, 0.5, and 0.1
676 kcal/ (mol $Å^2$)) or 2fs (for k_F of 0) integration time-step, PME for electrostatics interactions (47),
677 and were carried out in NPT ensemble under isotropic pressure coupling conditions, at a
678 temperature of 310 K. The Nose-Hoover Langevin piston algorithm (48) was used to control the
679 target P = 1 atm pressure with the "LangevinPistonPeriod" set to 200 fs and
680 "LangevinPistonDecay" set to 50 fs. The van der Waals interactions were calculated applying a
681 cutoff distance of 12 Å and switching the potential from 10 Å.

682 After this initial equilibration phase, the velocities of all atoms in the system were reset and
683 ensemble MD runs were initiated with OpenMM version 7.4 (49) during which the system was

684 simulated in 18 independent replicates, each for 640ns (i.e., cumulative time of ~11.5 μs for
685 each FP construct). These runs implemented PME for electrostatic interactions and were
686 performed at 310K temperature under NVT ensemble. In addition, 4fs time-step was used, with
687 hydrogen mass repartitioning and with "friction" parameter set to 1.0/picosecond. Additional
688 parameters for these runs included: "EwaldErrorTolerance" 0.0005, "rigidwater" True, and
689 "ConstraintTolerance" 0.000001. The van der Waals interactions were calculated applying a
690 cutoff distance of 12 Å and switching the potential from 10 Å.
691
692 **MD simulations of SARS-CoV-1 FP interactions with lipid membranes.** Interactions of selected
693 two models of the Calcium-bound WT SARS-CoV-1 FP with lipid membranes were investigated
694 with atomistic MD simulations. These runs were initiated by placing each of the models in the
695 proximity of a bilayer composed of 3:1:1 POPC/POPG/Cholesterol that had been pre-
696 equilibrated for 25ns as described previously (21).
697 After the FP-membrane complexes were embedded in a solution box (containing 150 mM
698 Na^+Cl^- salt concentration), each system was equilibrated with NAMD version 2.13 following the
699 same multi-step protocol described above during which the backbone atoms of the FP as well
700 as the Calcium ions were first harmonically constrained and subsequently gradually released in
701 four steps. After this phase, the velocities of all atoms of the system were reset, and ensemble
702 MD runs were initiated with OpenMM version 7.4. Each system was simulated in 18
703 independent replicates, each ran for ~ 1 μs (i.e., cumulative time of ~18 μs for each FP-
704 membrane complex). These runs implemented PME for electrostatic interactions and were
705 performed at 298K temperature under NPT ensemble using semi-isotropic pressure coupling,

706 with 4fs time-steps, using hydrogen mass repartitioning and with "friction" parameter set to
707 1.0/picosecond. Additional parameters for these runs included: "EwaldErrorTolerance" 0.0005,
708 "rigidwater" True, and "ConstraintTolerance" 0.000001. The van der Waals interactions were
709 calculated applying a cutoff distance of 12 Å and switching the potential from 10 Å. For all
710 simulations we used the latest CHARMM36 force-field for proteins and lipids (50), as well as the
711 recently revised CHARMM36 force-field for ions which includes non-bonded fix (NBFIX)
712 parameters for Na^+ and Calcium ions (51).
713

714 **Supporting Information**

715 **Figure S1** shows representative Spike immunoblots results of our Biotinylation Assays, which
716 we carried out with the wild-type and mutant SARS-CoV-1 constructs used in this study.
717 **Figure S2** shows the predicted models of calcium ions binding to the wild-type and single
718 charge-to-alanine mutants generated from the MD simulations.
719 **Figure S3** shows the predicted models of calcium ions binding to the wild-type and double
720 charge-to-alanine mutants generated from the MD simulations.
721 **Table 1** is a list of the primer sets used to generate the SARS-CoV-1 single and double mutants.
722

723 **Corresponding Author Information**

724 Susan Daniel, Ph.D., William C. Hooey Director & Fred H. Rhodes Professor of Chemical
725 Engineering, Robert Frederick Smith School of Chemical and Biomolecular Engineering
726 Cornell University | 124 Olin Hall, Ithaca, NY 14853 USA, phone: (607)255-4675, email:
727 sd386@cornell.edu

728

729 **Present/Current Author Addresses**

730 Javier A. Jaimes, Ph.D.

731 The University of Massachusetts Medical School, Program in Molecular Medicine, 373

732 Plantation Street, Biotech 2 Suite 319 Worcester MA 01605 USA, phone: (508)856-6891, email:

733 Javier.Jaimes@umassmed.edu

734

735 **Author Contributions**

736 Conceived and designed the experiments: MKB JDC GK MRS TT JAJ HW GRW SD. Performed the

737 experiments: JDC GK* MKB MRS TT. Analyzed the data: JDC GK MKB MRS TT JAJ HW GRW SD.

738 Wrote and edited the paper: JDC MKB GK MRS TT HW GRW SD. Acquired funding: GRW SD HW.

739 Computational Resources: HW GK.

740

741 **Acknowledgements**

742 We would like to thank members of the Daniel, Whittaker, and Abbott groups as well as the

743 Weinstein group at Weill Cornell for helpful discussions. This work was supported by The

744 National Institute of Health research grant R01AI35270, National Science Foundation RAPID

745 grant 2027070 and Fast Grant from the Mercatus Center at George Mason University. TT is

746 supported by the National Science Foundation Graduate Research Fellowship Program under

747 Grant No. DGE-1650441 and the Samuel C. Fleming Family Graduate Fellowship. H.W. and G.K.

748 gratefully acknowledge support from the 1923 Fund, and the access to computational

749 resources awarded through the COVID-19 High Performance Computing Consortium at the

750 Center for Computational Innovations (CCI) at the Rensselaer Polytechnic Institute and
751 Accounts BIP225 and BIP109 at the Oak Ridge Leadership Computing Facility, which is a DOE
752 Office of Science User Facility supported under Contract DE-AC05-00OR22725.

753 **Abbreviations Used**

754 Fusion Peptide (FP)

755 Spike (S)

756 Molecular Dynamics Simulations (MDS)

757 Coronaviruses (CoVs)

758

759 **References**

760

761 1. Lai MM, Cavanagh D. The molecular biology of coronaviruses. Adv Virus Res. 1997;48:1-
762 100.
763 2. Masters PS. The molecular biology of coronaviruses. Adv Virus Res. 2006;66:193-292.
764 3. Cherry JD, Krogstad P. SARS: the first pandemic of the 21st century. Pediatr Res.
765 2004;56(1):1-5.
766 4. de Groot RJ, Baker SC, Baric RS, Brown CS, Drosten C, Enjuanes L, et al. Middle East
767 respiratory syndrome coronavirus (MERS-CoV): announcement of the Coronavirus Study Group.
768 J Virol. 2013;87(14):7790-2.
769 5. Wu F, Zhao S, Yu B, Chen YM, Wang W, Song ZG, et al. A new coronavirus associated
770 with human respiratory disease in China. Nature. 2020;579(7798):265-9.
771 6. Zhou P, Yang XL, Wang XG, Hu B, Zhang L, Zhang W, et al. A pneumonia outbreak
772 associated with a new coronavirus of probable bat origin. Nature. 2020;579(7798):270-3.
773 7. de Wit E, van Doremalen N, Falzarano D, Munster VJ. SARS and MERS: recent insights
774 into emerging coronaviruses. Nat Rev Microbiol. 2016;14(8):523-34.
775 8. Shulla A, Heald-Sargent T, Subramanya G, Zhao J, Perlman S, Gallagher T. A
776 transmembrane serine protease is linked to the severe acute respiratory syndrome coronavirus
777 receptor and activates virus entry. J Virol. 2011;85(2):873-82.
778 9. Millet JK, Whittaker GR. Host cell proteases: Critical determinants of coronavirus
779 tropism and pathogenesis. Virus Res. 2015;202:120-34.
780 10. Stevens CS, Oguntuyo KY, Lee B. Proteases and variants: context matters for SARS-CoV-2
781 entry assays. Curr Opin Virol. 2021;50:49-58.

782 11. Matsuyama S, Ujike M, Morikawa S, Tashiro M, Taguchi F. Protease-mediated
783 enhancement of severe acute respiratory syndrome coronavirus infection. Proc Natl Acad Sci U
784 S A. 2005;102(35):12543-7.
785 12. Tang T, Bidon M, Jaimes JA, Whittaker GR, Daniel S. Coronavirus membrane fusion
786 mechanism offers a potential target for antiviral development. Antiviral Res. 2020;178:104792.
787 13. Belouzard S, Chu VC, Whittaker GR. Activation of the SARS coronavirus spike protein via
788 sequential proteolytic cleavage at two distinct sites. Proc Natl Acad Sci U S A.
789 2009;106(14):5871-6.
790 14. Bosch BJ, Bartelink W, Rottier PJ. Cathepsin L functionally cleaves the severe acute
791 respiratory syndrome coronavirus class I fusion protein upstream of rather than adjacent to the
792 fusion peptide. J Virol. 2008;82(17):8887-90.
793 15. Dube M, Rey FA, Kielian M. Rubella virus: first calcium-requiring viral fusion protein.
794 PLoS Pathog. 2014;10(12):e1004530.
795 16. Nathan L, Lai AL, Millet JK, Straus MR, Freed JH, Whittaker GR, et al. Calcium Ions
796 Directly Interact with the Ebola Virus Fusion Peptide To Promote Structure-Function Changes
797 That Enhance Infection. ACS Infect Dis. 2020;6(2):250-60.
798 17. Lai AL, Millet JK, Daniel S, Freed JH, Whittaker GR. The SARS-CoV Fusion Peptide Forms
799 an Extended Bipartite Fusion Platform that Perturbs Membrane Order in a Calcium-Dependent
800 Manner. J Mol Biol. 2017;429(24):3875-92.
801 18. Straus MR, Tang T, Lai AL, Flegel A, Bidon M, Freed JH, et al. Ca(2+) Ions Promote Fusion
802 of Middle East Respiratory Syndrome Coronavirus with Host Cells and Increase Infectivity. J
803 Virol. 2020;94(13).
804 19. Lai AL, Freed JH. SARS-CoV-2 Fusion Peptide has a Greater Membrane Perturbating
805 Effect than SARS-CoV with Highly Specific Dependence on Ca(2). J Mol Biol.
806 2021;433(10):166946.
807 20. Madu IG, Roth SL, Belouzard S, Whittaker GR. Characterization of a highly conserved
808 domain within the severe acute respiratory syndrome coronavirus spike protein S2 domain with
809 characteristics of a viral fusion peptide. J Virol. 2009;83(15):7411-21.
810 21. Khelashvili G, Plante A, Doktorova M, Weinstein H. Ca(2+)-dependent mechanism of
811 membrane insertion and destabilization by the SARS-CoV-2 fusion peptide. Biophys J.
812 2021;120(6):1105-19.
813 22. Madu IG, Belouzard S, Whittaker GR. SARS-coronavirus spike S2 domain flanked by
814 cysteine residues C822 and C833 is important for activation of membrane fusion. Virology.
815 2009;393(2):265-71.
816 23. Lai AL, Freed JH. Negatively charged residues in the membrane ordering activity of SARS-
817 CoV-1 and -2 fusion peptides. Biophys J. 2022;121(2):207-27.
818 24. Gui M, Song W, Zhou H, Xu J, Chen S, Xiang Y, et al. Cryo-electron microscopy structures
819 of the SARS-CoV spike glycoprotein reveal a prerequisite conformational state for receptor
820 binding. Cell Res. 2017;27(1):119-29.
821 25. Li F, Berardi M, Li W, Farzan M, Dormitzer PR, Harrison SC. Conformational states of the
822 severe acute respiratory syndrome coronavirus spike protein ectodomain. J Virol.
823 2006;80(14):6794-800.

824 26. Millet JK, Tang T, Nathan L, Jaimes JA, Hsu HL, Daniel S, et al. Production of Pseudotyped
825 Particles to Study Highly Pathogenic Coronaviruses in a Biosafety Level 2 Setting. J Vis Exp.
826 2019(145).
827 27. Tang T, Jaimes JA, Bidon MK, Straus MR, Daniel S, Whittaker GR. Proteolytic Activation
828 of SARS-CoV-2 Spike at the S1/S2 Boundary: Potential Role of Proteases beyond Furin. ACS
829 Infect Dis. 2021;7(2):264-72.
830 28. Gu J, Korteweg C. Pathology and pathogenesis of severe acute respiratory syndrome.
831 Am J Pathol. 2007;170(4):1136-47.
832 29. Ding Y, Wang H, Shen H, Li Z, Geng J, Han H, et al. The clinical pathology of severe acute
833 respiratory syndrome (SARS): a report from China. J Pathol. 2003;200(3):282-9.
834 30. Wang H, Yang P, Liu K, Guo F, Zhang Y, Zhang G, et al. SARS coronavirus entry into host
835 cells through a novel clathrin- and caveolae-independent endocytic pathway. Cell Res.
836 2008;18(2):290-301.
837 31. Singh P, Mukherji S, Basak S, Hoffmann M, Das DK. Dynamic Ca(2+) sensitivity stimulates
838 the evolved SARS-CoV-2 spike strain-mediated membrane fusion for enhanced entry. Cell Rep.
839 2022;39(3):110694.
840 32. Lai AL, Freed JH. SARS-CoV-2 Fusion Peptide has a Greater Membrane Perturbating
841 Effect than SARS-CoV with Highly Specific Dependence on Ca2+. Journal of Molecular Biology.
842 2021;433(10):166946.
843 33. Khelashvili G, Plante A, Doktorova M, Weinstein H. Ca^{2+}-dependent mechanism of
844 membrane insertion and destabilization by the SARS-CoV-2 fusion peptide. Biophysical Journal.
845 2021;120(6):1105-19.
846 34. Cai Y, Zhang J, Xiao T, Peng H, Sterling SM, Walsh RM, Jr., et al. Distinct conformational
847 states of SARS-CoV-2 spike protein. Science. 2020;369(6511):1586-92.
848 35. Koppisetti RK, Fulcher YG, Van Doren SR. Fusion Peptide of SARS-CoV-2 Spike
849 Rearranges into a Wedge Inserted in Bilayered Micelles. J Am Chem Soc. 2021;143(33):13205-
850 11.
851 36. Schaefer SL, Jung H, Hummer G. Binding of SARS-CoV-2 Fusion Peptide to Host
852 Endosome and Plasma Membrane. J Phys Chem B. 2021;125(28):7732-41.
853 37. Straus MR, Bidon MK, Tang T, Jaimes JA, Whittaker GR, Daniel S. Inhibitors of L-Type
854 Calcium Channels Show Therapeutic Potential for Treating SARS-CoV-2 Infections by Preventing
855 Virus Entry and Spread. ACS Infect Dis. 2021;7(10):2807-15.
856 38. Crespi B, Alcock J. Conflicts over calcium and the treatment of COVID-19. Evol Med
857 Public Health. 2021;9(1):149-56.
858 39. Danta CC. Calcium Channel Blockers: A Possible Potential Therapeutic Strategy for the
859 Treatment of Alzheimer's Dementia Patients with SARS-CoV-2 Infection. ACS Chem Neurosci.
860 2020;11(15):2145-8.
861 40. Straus MR, Bidon M, Tang T, Whittaker GR, Daniel S. FDA approved calcium channel
862 blockers inhibit SARS-CoV-2 infectivity in epithelial lung cells. bioRxiv. 2020:2020.07.21.214577.
863 41. Korber B, Fischer WM, Gnanakaran S, Yoon H, Theiler J, Abfalterer W, et al. Tracking
864 Changes in SARS-CoV-2 Spike: Evidence that D614G Increases Infectivity of the COVID-19 Virus.
865 Cell. 2020;182(4):812-27 e19.
866 42. Li Q, Wu J, Nie J, Zhang L, Hao H, Liu S, et al. The Impact of Mutations in SARS-CoV-2
867 Spike on Viral Infectivity and Antigenicity. Cell. 2020;182(5):1284-94 e9.

868 43. Olsson MH, Sondergaard CR, Rostkowski M, Jensen JH. PROPKA3: Consistent Treatment
869 of Internal and Surface Residues in Empirical pKa Predictions. J Chem Theory Comput.
870 2011;7(2):525-37.
871 44. Olsson MHM, Søndergaard CR, Rostkowski M, Jensen JH. PROPKA3: Consistent
872 Treatment of Internal and Surface Residues in Empirical pKa Predictions. Journal of Chemical
873 Theory and Computation. 2011;7(2):525-37.
874 45. Humphrey W, Dalke A, Schulten K. VMD: visual molecular dynamics. J Mol Graph.
875 1996;14(1):33-8, 27-8.
876 46. Phillips JC, Braun R, Wang W, Gumbart J, Tajkhorshid E, Villa E, et al. Scalable molecular
877 dynamics with NAMD. J Comput Chem. 2005;26(16):1781-802.
878 47. Essmann U, Perera L, Berkowitz ML, Darden T, Lee H, Pedersen LG. A smooth particle
879 mesh Ewald method. The Journal of Chemical Physics. 1995;103(19):8577-93.
880 48. Evans DJ, Holian BL. The Nose–Hoover thermostat. The Journal of Chemical Physics.
881 1985;83(8):4069-74.
882 49. Eastman P, Swails J, Chodera JD, McGibbon RT, Zhao Y, Beauchamp KA, et al. OpenMM
883 7: Rapid development of high performance algorithms for molecular dynamics. PLoS Comput
884 Biol. 2017;13(7):e1005659.
885 50. Huang J, Rauscher S, Nawrocki G, Ran T, Feig M, de Groot BL, et al. CHARMM36m: an
886 improved force field for folded and intrinsically disordered proteins. Nature Methods.
887 2017;14(1):71-3.
888 51. Venable RM, Luo Y, Gawrisch K, Roux B, Pastor RW. Simulations of anionic lipid
889 membranes: development of interaction-specific ion parameters and validation using NMR
890 data. J Phys Chem B. 2013;117(35):10183-92.
891

892

893

894

895

896

897

898

899

900

901
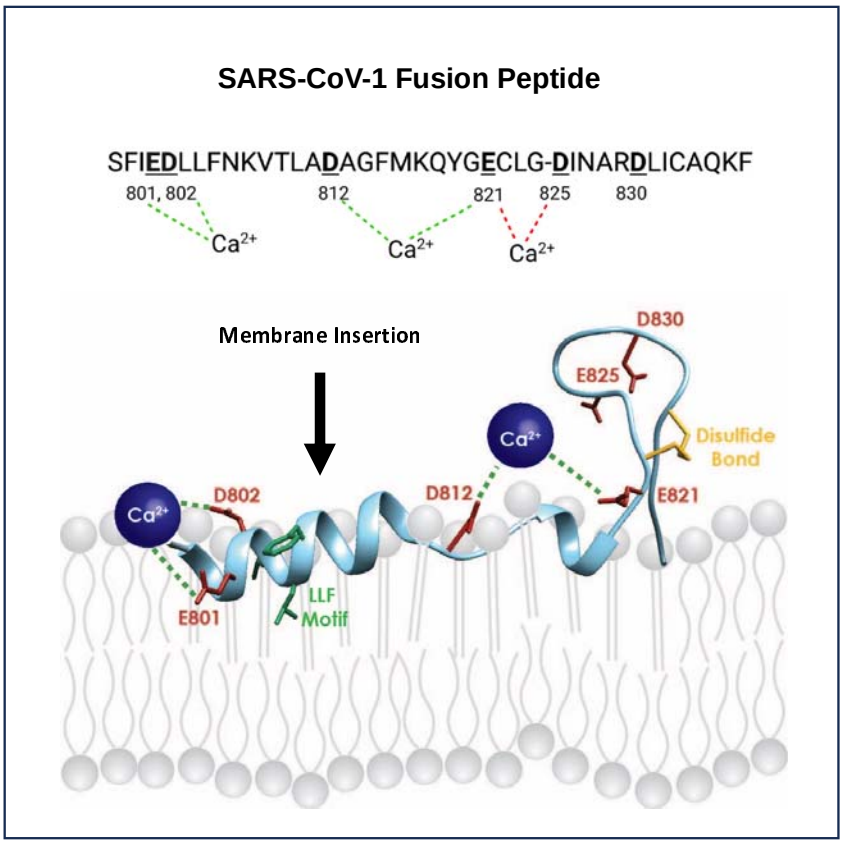
For Table of Contents Only